Metallomics

MicroXRF tomographic visualization of zinc and iron in the zebrafish embryo at the onset of the hatching period

Journal:	*Metallomics*
Manuscript ID	MT-ART-03-2016-000073.R2
Article Type:	Paper
Date Submitted by the Author:	02-Jul-2016
Complete List of Authors:	Bourassa, Daisy; Georgia Institute of Technology, Chemistry + Biochemistry Gleber, Sophie-Charlotte; Argonne National Laboratory, X-ray Science Division Vogt, Stefan; Argonne National Laboratory, X-ray Science Division Yi, Hong; Emory University, c. Robert P. Apkarian Integrated Electron Microscopy Core Shin, Chong; Georgia Institute of Technology, Biology Fahrni, Christoph; Georgia Institute of Technology, Chemistry + Biochemistry

Metallomics

ARTICLE

MicroXRF tomographic visualization of zinc and iron in the zebrafish embryo at the onset of the hatching period

Received 00th January 20xx,
Accepted 00th January 20xx

DOI: 10.1039/x0xx00000x

www.rsc.org/

Daisy Bourassa,[a] Sophie-Charlotte Gleber,[b] Stefan Vogt,[b] Hong Yi,[c] Chong Hyun Shin,[d] and Christoph J. Fahrni*[a]

Transition metals such as zinc, copper, and iron play key roles in cellular proliferation, cell differentiation, growth, and development. Over the past decade, advances in synchrotron X-ray fluorescence instrumentation presented new opportunities for the three-dimensional mapping of trace metal distributions within intact specimens. Taking advantage of microXRF tomography, we visualized the 3D distribution of zinc and iron in a zebrafish embryo at the onset of the hatching period. The reconstructed volumetric data revealed distinct differences in the elemental distributions, with zinc predominantly localized to the yolk and yolk extension, and iron to various regions of the brain as well as the myotome extending along the dorsal side of the embryo. The data set complements an earlier tomographic study of an embryo at the pharyngula stage (24 hpf), thus offering new insights into the trace metal distribution at key stages of embryonic development.

Introduction

Zinc, copper, and iron are vital trace nutrients for most forms of life. As components of enzymes and proteins, they are essential to many primary biological functions and play critical roles in cellular proliferation, differentiation, and embryonic development. For example, zinc is essential for the mitotic and meiotic cell cycle progression[1] and plays an important role for proper development of the fetus and neonate.[2] Similarly, copper and iron are critical during pregnancy where an inadequate nutritional supply could have damaging effects on fetal and neonatal development.[3] While zinc, copper, and iron are key constituents for the maintenance of primary biological functions in all cells, some organs and tissues pose an increased demand for one or more of these trace nutrients in order to fulfill their specialized roles.[4] A developing embryo is therefore not only required to guarantee a sufficient dietary intake but also to redistribute trace nutrients in order to satisfy specialized biochemical demands in the course of development. Despite the established importance of transition metals during development, mechanisms responsible for their redistribution remain elusive.

Zebrafish (*Danio rerio*) represent an ideal model system to study the trace metal distribution during early embryogenesis. As a lecithotrophic organism, zebrafish relies only on the nutrition of the yolk during the early stages of development,[5] and the embryo can survive on this nutrition source for the first 3 to 4 days before requiring exogenous feeding.[6] Starting out as a single-cell zygote, the embryo transitions through various developmental stages characterized by distinct morphologies, including the cleavage, blastula, gastrula, segmentation, pharyngula, and hatching periods.[7] Throughout this process, nutrients stored in the yolk must be redistributed to meet the varying demands of the developing organs and tissues.

Synchrotron x-ray fluorescence (SXRF) microscopy is a powerful technique to visualize trace metal distributions in biological specimens with submicron resolution.[8] Recent progress in X-ray imaging technology, notably fly-scan data acquisition and improved detector sensitivity, significantly reduced data collection times and paved the way towards visualizing 3-dimensional elemental distributions based on tomographic approaches.[9] We recently employed SXRF micro-tomography to image the 3D elemental distribution of zinc, iron and copper in a zebrafish embryo at the pharyngula stage 24 hours post fertilization (hpf).[10] In order to preserve the native elemental composition, the embryo was embedded at cryo-temperature in a methacrylate-based resin. Beam attenuation by the resin matrix was minimized by excising the specimen through femtosecond laser sectioning prior to mounting on the tomographic sample stage. Based on 60 tomographic projections acquired over 100 hours of beam time, we were able to reconstruct the corresponding 3D elemental volumes using a maximum likelihood expectation maximization (MLEM) algorithm. Encouraged by this study, we sought to expand the tomographic visualization of trace elements to other key stages of embryonic development.[11] In

[a] *School of Chemistry and Biochemistry and Petit Institute for Bioengineering and Bioscience, Georgia Institute of Technology, 901 Atlantic Drive, Atlanta, GA 30332, USA. E-mail: fahrni@chemistry.gatech.edu.*
[b] *Advanced Photon Source, X-ray Science Division, Argonne National Laboratory, 9700 S. Cass Avenue, Argonne, IL 60439, USA.*
[c] *Robert P. Apkarian Integrated Electron Microscopy Core, Emory University, 1521 Dickey Drive, Atlanta, GA 30322, USA*
[d] *School of Biology and Petit Institute for Bioengineering and Bioscience, Georgia Institute of Technology, 315 Ferst Drive, Atlanta, GA 30332, USA*

this report, we studied embryos at 48 hpf, the onset of the hatching period where the morphogenesis of the primary organ system, such as the liver and heart, as well as distinct features of the lens and retina can be observed.[7] Compared to the pharyngula stage at 24 hpf, the head appears larger while the yolk sac and yolk extension are being depleted, the pericardial cavity and the developing atrium of the heart become visible,[12] and the eyes are rendered more prominent as the lens is detached from the retina.[13]

Experimental

Specimen preparation

Adult wild-type zebrafish were housed under standard laboratory conditions. Fertilized embryos were harvested and kept at 28.5°C in an E3 salt medium (5 mM NaCl, 0.17 mM KCl, 0.4 mM $CaCl_2$ and 0.16 mM $MgSO_4$) without supplementation of transition metals. At 48 hpf, embryos were anaesthetized in 0.02% Tricaine (Sigma, E10521), manually dechorionated, and fixed for 2 hours with a 4% paraformaldehyde solution. The fixative was washed away with a 0.1 M sodium phosphate buffer (PBS). Following the previously developed approach for the preparation of X-ray compatible soft tissue specimens,[10] the embryos were embedded in Lowicryl K4M resin at –35°C following the progressive lowering of temperature (PLT) method (ESI).[14] The specimens were excised from the resin with a laser-based microtome system (TissueSurgeon, LLS Rowiak, LaserLabSolutions GmbH, Hannover, Germany), which allowed for contact-free three-dimensional cutting with micrometer precision without affecting the integrity of the specimens.[10] To minimize attenuation of the excitation beam and emitted photons, the resin block was trimmed at a distance of 40-60 µm from the specimen, thus yielding a cuboid with the dimensions of 0.5 x 0.8 x 2.8 mm. The integrity of the specimen after laser cutting was confirmed through a series of brightfield phase-contrast images.

Data acquisition

Tomographic X-ray fluorescence data were acquired at the 2-ID-E beam line of the Advanced Photon Source (Argonne National Laboratory, USA). The microtomography instrument is equipped with a Fresnel zone plate optics, which focuses the incident beam to a spot size of 0.5 x 0.6 μm^2, and a 4-element fluorescence detector positioned at a 90 degree angle to the beam trajectory. A detailed description of the instrument has been reported previously.[10] A set of 60 tomographic X-ray fluorescence projections were collected at room temperature with 3 degree intervals through raster scanning of the specimen block through the incident beam with excitation at 10 keV and a uniform horizontal and vertical step size of 3.5 µm.

Data processing and tomographic reconstruction

Elemental maps were generated using the MAPS software package[15] utilizing Gaussian fitting of the averaged raw emission spectra. The Gaussian peaks were matched to the characteristic X-ray emission lines to determine the fluorescence signal for Zn, Cu, and Fe. Calibration to elemental densities was performed by comparing the fluorescence emission of the sample with that of a thin film standard (AXO Dresden, Germany) relative to the photon flux captured by two ion chambers positioned upstream and downstream of the sample. The 3D elemental distributions were reconstructed based on a MLEM algorithm implemented in MATLAB[16] and a linear attenuation correction was employed as described in the Results and Discussion section.

Data visualization

Volumetric renderings were generated with the Paraview software package.[17] For this purpose, the reconstructed volumetric data were exported from MATLAB as 32-bit z-stacks, converted to 16-bit stacks using ImageJ,[18] and then imported into Paraview for 3D processing and visualization.

Results and Discussion

For accurate tomographic reconstruction, the structural integrity of the specimen must be maintained during the entire data acquisition period for several days. Among various preservation protocols, cryo-fixation would be the preferred choice to retain the native distribution of trace metals;[19] however, initial attempts to cryopreserve the embryos through high-pressure freezing[20] led to fragmentation, likely due to insufficient cooling rates for this size of specimen. We therefore employed the progressive lowering of temperature (PLT) method for cryo-embedding in Lowicryl K4M, a low-viscosity polar resin that can be polymerized at subzero temperatures by long-wave UV irradiation. Introduced by Carlemalm et al. in 1982,[14] this embedding method retains the molecular order of protein crystals within 0.6 to 0.8 nm and preserves their antigenicity for immunocytochemical labeling. By subjecting the aldehyde-fixed specimen to increasing concentrations of ethanol while progressively lowering the temperature, the formation of damaging ice crystals is avoided. Subsequent infiltration with Lowicryl resin and UV-mediated polymerization at –35°C does not remove the hydration shell of proteins and thus preserves the specimen in a more natural state compared to room temperature embedding protocols. Although we would expect that the spatial organization of protein-bound trace metal ions such as Zn, Fe, or Cu are retained during the embedding process, we also do not exclude the possibility of artifacts caused by leaching or redistribution of a labile subpool. At present, there are no data available to gauge the effect of low-temperature embedding on the metal ion content in zebrafish embryos. A recent comparison of various sample preparation methods showed that mild chemical fixation with paraformaldehyde of cells and tissues yielded good reproducibility for the Zn, Fe, and Cu contents,[19,21] thus offering some confidence that PLT cryo-embedding in Lowicryl may preserve the original distribution of non-labile trace metal ions in the specimen.

To minimize signal attenuation by the resin matrix, the specimens were excised from the resin block using a femtosecond laser-based microtome,[10] and glued along the axial direction to an aluminum stick for mounting on the kinematic stage of the microtomography instrument. X-ray fluorescence tomographic projections were acquired at room temperature over an angular space of 180 degrees at 3 degrees intervals and a raster-scan resolution of 3.5 µm, resulting in a total of 60 projections collected during 110 hours of beam time. Although the Fresnel zone plate optics of the instrument would offer, in principle, a 40-fold finer raster-scan grid, the resulting data acquisition time would have been prohibitively long. Given the large size of the specimen, the spatial resolution of the current data set was therefore not limited by the X-ray optics but rather determined by the available beam time and the minimum signal-to-noise ratio required for a reliable reconstruction of the 3D elemental distribution. Judging from the integrated photon count, which remained stable for each trace element throughout the data acquisition period, the radiation damage of inorganic material appeared negligible.

Due to attenuation of the excitation and fluorescence emission by the Lowicryl resin, the actual elemental content is underestimated by the detected photon counts when referenced to a thin film standard. For this reason, we applied element-specific linear attenuation corrections to approximate the actual metal ion concentrations (see ESI). Despite its simplicity, previous attenuation simulations indicate that the corrected concentrations of Zn, Cu, and Fe should be accurate within an error margin of 20% or better for this size of specimens.[10] The linear attenuation coefficient μ_{ex} for excitation at 10 keV and the average path length of the matrix were determined based on the difference of the photon flux before and after passing through the specimen. As illustrated with Figure 1, the intensity of the incident beam drops by approximately 20% if the resin block is positioned at 0° or 180° relative to the incoming beam, and by approximately 30% at angle of 90°. On the basis of these data, we determined an average attenuation coefficient μ_{ex} (10 keV) for Lowicryl of 4.07 ± 0.09 cm^{-1}, a value that is in good agreement with previous measurements.[10] The attenuation coefficients for the element-specific Kα emissions of Zn, Cu, and Fe were calculated with the software WinXCOM based on the density and elemental composition of Lowicryl reported by Reichelt *et al.* (ρ = 1.24 g/cm^3; weight fractions C 59.2%, O 32.3%, H 8.43%)[22] to yield the values $\mu_{ZnK\alpha}$ = 6.41 cm^{-1}, $\mu_{CuK\alpha}$ = 7.91 cm^{-1}, and $\mu_{FeK\alpha}$ = 15.75 cm^{-1}, respectively.

Figure 2 illustrates the energy-dependent attenuations of the excitation beam and the Kα emissions of Zn, Cu, and Fe as a function of the path length through the matrix based on the estimated attenuation coefficients. The corresponding attenuation length, defined as the depth into a material where the X-ray intensity falls to 1/e of the initial value (37%), decreases from 2.5 mm for the incident beam to 0.67 mm for the Kα emission of Fe. Altogether, these data demonstrate that Lowicryl is quite well-suited as an X-ray compatible matrix material for imaging the biologically relevant first-row transition elements in specimens of up to approximately 1 mm of thickness.

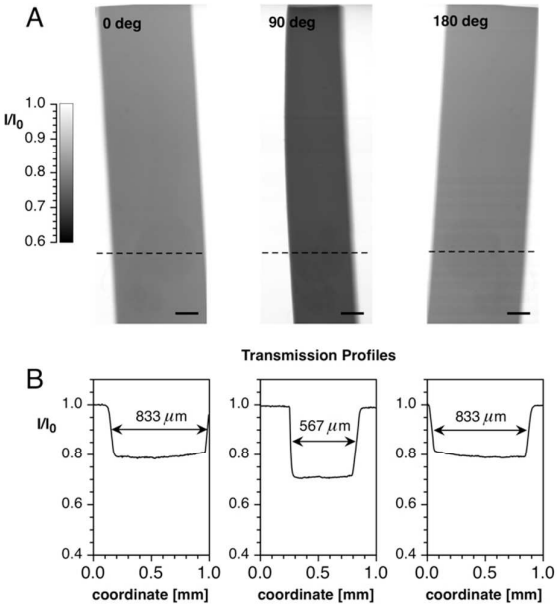

Figure 1: Attenuation of the incident X-ray beam (10 keV) by the Lowicryl resin matrix. A) Absorption contrast images of the resin block at 0°, 90°, and 180° orientations relative to the incident beam. Scale bar: 200 µm. B) Transmission profiles across the image coordinate marked with a dashed line in panel (A). Note that attenuation by the zebrafish embryo is negligible compared to the matrix material.

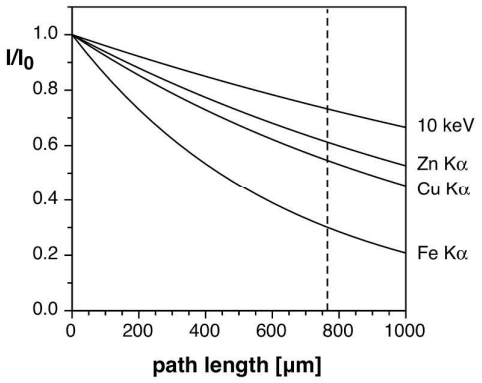

Figure 2: Energy-dependent attenuation of photons passing through a PMMA matrix as a function of path length, calculated according to equation (1). The following attenuation coefficients were used for the plot: μ_{10keV} = 4.07 cm^{-1}, $\mu_{ZnK\alpha}$ = 6.41 cm^{-1}, $\mu_{CuK\alpha}$ = 7.91 cm^{-1}, and $\mu_{FeK\alpha}$ = 15.75 cm^{-1}. The dashed line indicates the average path length of the resin matrix (l = 760 µm).

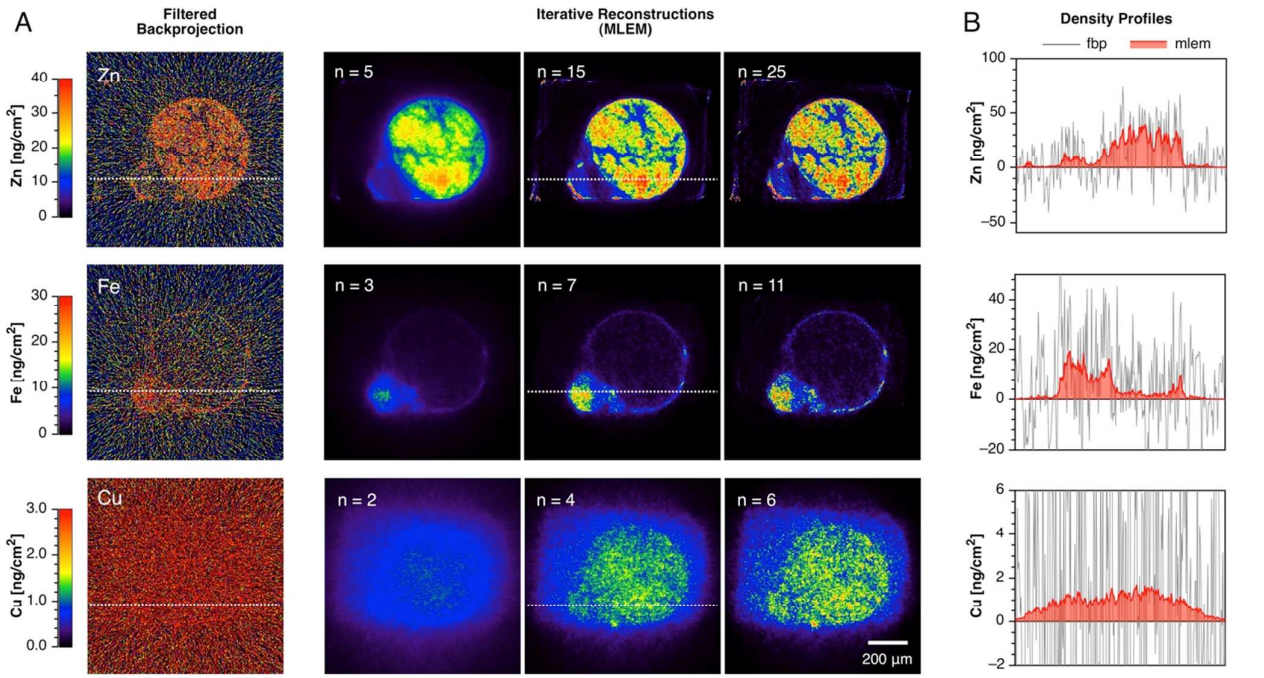

Figure 3: Tomographic reconstruction of the elemental densities of Zn, Fe, and Cu based on a single-line sinogram using an iterative MLEM algorithm. (A) Comparison of the reprojected elemental densities based on filtered back projection with Ramachandran–Lakshminarayanan (''Ram–Lak'') ramp-filter and the MLEM algorithm. The latter leads to significantly improved reconstructions for noisy data sets. (B) Density profiles of the reconstructed images shown in (A) along the white dashed line. The fluorescence detector was positioned on the left side relative to the reconstructed images in panel (A).

Tomographic reconstruction

Compared to absorption-based X-ray computed tomography (CT), the signal-to-noise ratio of fluorescence tomography data is inherently much lower. For this reason, we utilized a standard iterative maximum likelihood expectation maximization (MLEM) algorithm for the reconstruction of the 3D elemental distributions. Originally developed for the analysis of positron emission tomography (PET) data, this algorithm assumes a Poisson distribution of the photon statistics and is significantly more noise-tolerant compared to filtered back projection (FBP) routinely used in X-ray CT. Although the MLEM algorithm approaches convergence with increasing iteration numbers, there is also a concomitant increase of the noise amplitude. For this reason, the optimal iteration number differs depending on the noise level of the raw sinogram and must be determined empirically. As illustrated with Figure 3, MLEM reconstruction of a line-sinogram of the Zn Kα emission in the yolk region of the zebrafish embryo yielded after a few iterations (n = 5) a density plot with rather soft contours, which significantly sharpened at higher iteration numbers. Based on the reconstructed density plots, we determined that a total of 15 iterations yielded the best compromise between sharpness and noise level. Due to the lower signal-to-noise ratio of the Fe Kα emission sinogram, the optimal MLEM iteration number of n = 7 was found to be smaller compared to the Zn data set. As the total amount of Cu in most organisms is approximately by one order of magnitude lower compared to Zn and Fe, it is not surprising that the signal-to-noise ratio of the Cu Kα emission sinogram is much lower compared to the Fe and Zn data. Concluding from the MLEM reconstructions shown in Figure 3,

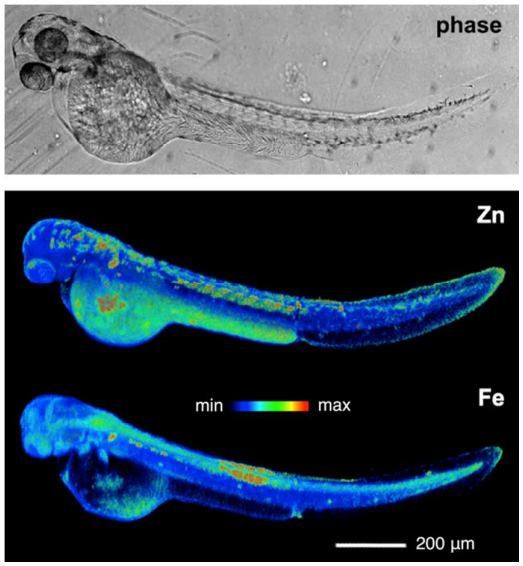

Figure 4: Zinc and iron distribution within the zebrafish embryo at 48 hpf, reconstructed on the basis of 60 tomographic projections using an iterative MLEM algorithm. The false-color calibration bar reflects a dynamic range from 0-2 mM for Zn and 0-1 mM for Fe. For comparison, the phase image (top) shows the resin-embedded embryo along the same projection axis.

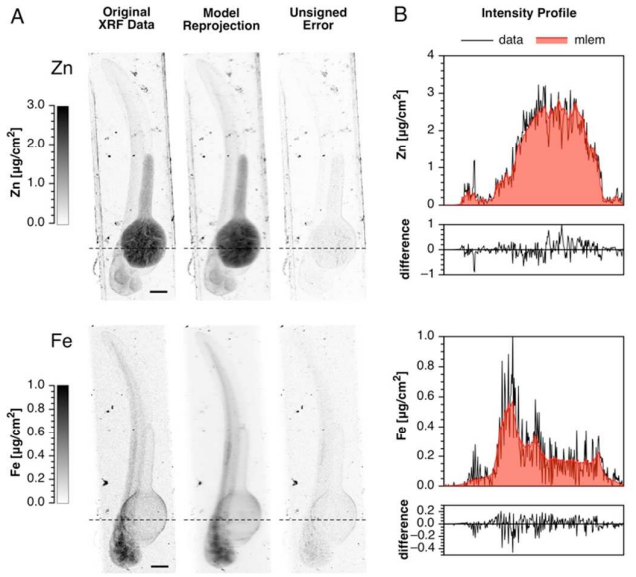

Figure 5: Comparison of the experimental and reconstructed elemental densities at a projection angle of 0 degree. A) The volumetric distribution of each element was reconstructed using an iterative MLEM algorithm, and the volumetric data were reprojected at the same angle as the measured data set (2nd column). The 3rd column illustrates the unsigned error in the form of difference images. The panels for each element are based on different density scale as indicated by the calibration bars on the left. B) Intensity profiles of the experimental (black) and reconstructed data (red) across the dashed line indicated in the projection images. The graph below each profile illustrates the signed difference between the experimental and reconstructed profiles

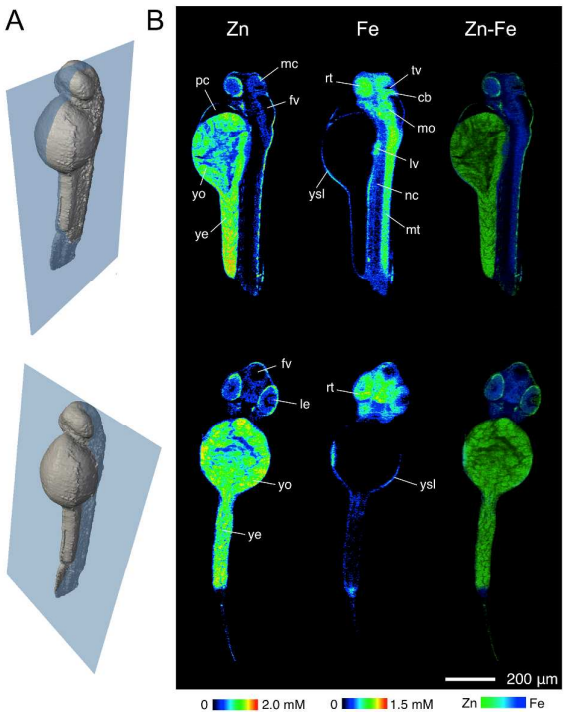

Figure 6: Visualization of elemental distribution in a zebrafish embryo (48 hpf) by X-ray fluorescence tomography using MLEM reconstruction. **A.** 3D-rendering of the embryo indicating the spatial orientation of the virtual slices that are displayed in panel B. Slices include a sagittal section (top) and a coronal section (bottom). **B.** Elemental distributions of Zn and Fe for each of the 2 slices. Individual concentration scales for each element are displayed at the bottom of each column. Abbreviations: Mesencephalon (mc), retina (rt), third ventricle (tv), cerebellum (cb), fourth ventricle (fv), pericardial cavity (pc), yolk (yo), yolk extension (ye), yolk syncytial layer (ysl), medulla oblongata (mo), liver (lv), notochord (nc), myotome (mt), and lens (le). The third column contains false-color overlays of the elemental distributions of Zn and Fe indicating regions of colocalization. The concentration scales of each element were normalized and color-coded as Zn (green) and Fe (blue). Areas of colocalization appear in the corresponding mixed hue.

the number of photons collected within the Cu Kα spectral region was insufficient to arrive at meaningful elemental densities, regardless of the number of iterations. By comparison, filtered back projection of the same set of sinograms resulted in reconstructed densities with much higher noise amplitudes, to the extent that the noise partially or completely obscured the elemental density distributions in the reconstructed images (Figure 3).

After identifying the optimal number of iterations, we applied the MLEM algorithm to each of the 815 line-sinograms to generate complete 3D elemental distributions for Zn and Fe (Figure 4). To arrive at actual elemental concentrations, the raw photon counts were compared with the emission intensity of a thin film standard containing known amounts of Zn, Cu, and Fe. Furthermore, we applied the corresponding linear scaling factors as described in the previous paragraph to compensate for signal attenuation by the Lowicryl resin. Based on the calibrated volumetric data, which entail over 63 million voxels with the dimension of 3.5 x 3.5 x 3.5 μm^3, we determined a total Zn content of ~8.2 ng. This value is in good agreement with the average Zn content reported in the literature for an embryo at this stage of development.[23] A comparison with the raw data acquired at the same projection angle revealed overall small deviations as evident from the corresponding difference images. As illustrated by the intensity profile shown in Figure 5B, the error was dominated by the increased noise-amplitude of the unprocessed data rather than a systematic deviation due to reconstruction artifacts.

3D elemental distribution

The reconstructed volumetric data shown in Figure 4 reveal distinct differences in the Zn and Fe distributions, most notably regions of elevated concentrations appear mutually exclusive. While the highest levels of zinc are found in the yolk sac and yolk extension, the iron concentration in both regions remains low. Conversely, areas with increased iron levels, including the myotome, extending along the dorsal side, or various regions of the brain, are consistently low in zinc. To provide a more detailed picture of the elemental localizations and how these regions relate to specific anatomical features,[11] Figure 6 and Figure 7 reveal a series of virtual sagittal, coronal and transverse sections of the embryo. The 3D renderings in

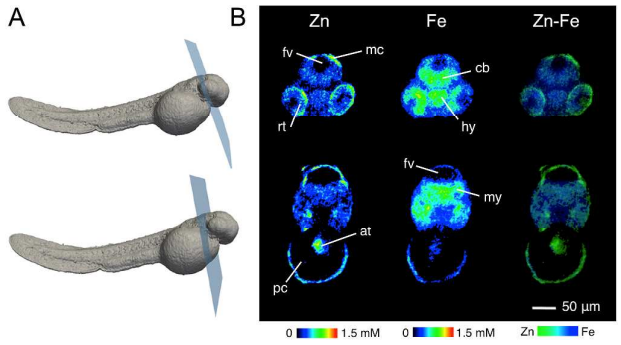

Figure 7: Visualization of elemental distribution in a zebrafish embryo (48 hpf) by X-ray fluorescence tomography using MLEM reconstruction. **A.** 3D-rendering of the embryo indicating the spatial orientation of the two virtual transverse slices that are displayed in panel B. **B.** Elemental distributions of Zn and Fe for each of the 2 slices. Individual concentration scales for each element are displayed at the bottom of each column. Abbreviations: Fourth ventricle (fv), mesencephalon (mc), retina (rt), cerebellum (cb), hypothalamus (hy), pericardial cavity (pc), atrium (at), and myelencephalon (my). The third column contains false-color overlays of the elemental distributions of Zn and Fe indicating regions of colocalization. The concentration scales of each element were normalized and color-coded as Zn (green) and Fe (blue). Areas of colocalization appear in the corresponding mixed hue.

column A represent isodensity surfaces of Zn to illustrate the position of each section corresponding to the 2D elemental maps arranged in column B. The yolk and yolk extension constitute approximately 83% of the total Zn content in the embryo at this stage of development. High levels of Zn, which range between 0.5 and 1.5 mM, are evident in both the sagittal and coronal sections depicted in Figure 6. Throughout the yolk, blood vessels can be readily located based on regions with markedly lower Zn levels averaging around 0.3-0.4 mM (Figure 6). Contrary to expectations, blood vessels do not appear in the Fe map as distinct features. Rather, a concentration profile across the yolk reveals uniform and low levels around 50 µM (Figure S1, ESI), a value that is close to the threshold of detection. At present, it is unclear whether yolk Fe levels are inherently low at this stage of development or whether the PLT cryo-embedding protocol might have resulted in a significant loss. In zebrafish, primitive hematopoietic cells begin to appear in the intermediate cell mass (IMS) already between 12 to 24 hpf, heme synthesis is initiated around 22 hpf, and immature blood cells start to circulate through the yolk at about 24 hpf.[24] Based on these data, the density of erythrocytes is expected to be lower compared to an adult fish; however, it remains surprising that the resulting Fe levels in the yolk reside at the limit of detection. In contrast, the yolk syncytial layer (YSL) exhibits a higher concentration of Fe, likely due to enhanced expression of the Fe transporters ferroportin1 and transferrin in the YSL.[25] A blue-green false-color overlay indicates strong anti-correlation between the Fe (blue) and Zn (green) levels throughout this region of the embryo (Figure 6B, right panel), an observation that is similar to the elemental distribution found at 24 hpf.[10] Anterior to the yolk sac, the pericardial cavity is notably void of both Zn and Fe. This cavity is filled with pericardial fluid, which is composed primarily of lactate dehydrogenase and other non-metalloproteins.[26] Additionally, transverse sectioning of the elemental reconstructions in Figure 7 reveals the single atrium of the heart. Based on the overlay image of both Zn and Fe, the atrium is rich in Zn. Moreover, the liver appears as a prominent, Fe-rich anatomical feature of the 48 hpf embryo. At this stage of embryogenesis, liver morphogenesis is well underway and is characterized by visible liver rudiments, continued budding, and the early formation of the hepatic duct.[27] As a major storage site of ferritin,[28] the primary protein responsible for intracellular Fe storage and release,[29] this organ is readily identified in the Fe distribution map. In contrast, at 24 hpf the zebrafish liver is described as a rudimentary endodermal rod in the pharyngeal region and cannot be readily recognized within the elemental distributions previously reported for this stage of development.[10]

The development of the lens and the retina also give rise to distinct differences in the elemental maps at 24 hpf compared to 48 hpf. In the embryo at 48 hpf, the lens has detached from the overlying ectoderm and developed into a large spherical structure separate from the retina.[30] These structures are easily distinguished in the reconstructions due to the elevated concentrations of Zn and Fe. Notably, the Zn distribution map indicates higher levels of Zn in the outer layers of the retina with concentrations ranging between 1 and 1.5 mM. Consistent with this observation, in situ hybridization imaging studies also revealed high levels of metallothionein transcripts in the retina of zebrafish embryos at 48 hpf.[31] The critical role of Zn and Fe in the normal function of the lens and retina is well established.[32] For example, high concentrations of histochemically reactive Zn have been identified in the mouse and rat retina, with the highest levels localized to the retinal pigment epithelium and the inner segment of the photo receptors.[33,34] These areas also coincide with increased expressions of the Zn transporters ZnT-3 and ZnT-7, [34,35] thus underscoring the importance of retinal zinc homeostasis, not only for the metallation of Zn-dependent proteins critical to vision,[36] but likely also for supporting the role of Zn as a neuromodulator.[37] SXRF microscopy studies on 30 µm-thick freeze-dried cryosections of rat retina indicated a similar distribution with increased Zn concentrations in the retinal pigment epithelium as well as the photoreceptor inner segment and outer limiting membrane.[38] Although these studies also revealed increased levels of Fe in the outer layers, our results show a more uniform distribution throughout this region. Similarly, high levels of Fe in the retinal epithelium are consistent with the presence of several Fe-dependent enzymes critical for cellular function, most notably the retinoid isomerohydrolase RPE65, an iron-dependent microsomal enzyme responsible for converting trans-retinyl ester to 11-cis retinol during the visual cycle.[39]

Dorsal to the lens and retina, high concentrations of both Zn and Fe define the grey and white matter of the brain, a region that contrasts the low trace metal concentrations found in the ventricles. The medulla oblongata, hypothalamus, myelencephalon, and mesencephalon including the cerebellum as well as the third and fourth ventricle can all be distinguished in both elemental maps. Similar to studies performed on human brain tissue,[40] the concentrations of Zn

and Fe show variability as they are heterogeneously distributed throughout different regions of the brain. As a major metal repository and one of the brain structures richest in Fe and Zn[40,41] it is not surprising that the cerebellum stands out in both sagittal and transverse sections of the elemental maps. Additionally, intracellular concentrations of Zn and Fe are critical for the normal function of the brain,[42,43] and are tightly regulated by a number of importers, exporters, and storage proteins. For example, iron regulatory proteins, ferritin and transferrin are found in the grey and white matter of the brain.[43,44] Although Fe uptake into the brain remains essential throughout life, it peaks during embryogenesis as demonstrated in rat by the rapid growth and development of this organ.[45] Furthermore, studies of the central nervous system in adult zebrafish revealed high levels of histochemically reactive Zn in the midbrain and hindbrain regions.[46]

Lastly, the posterior body of the embryo is largely defined by the tail and notochord. The notably low metal content in the notochord is an intriguing observation for a structure often characterized as an essential organ in development.[47] This finding also parallels the low trace metal concentration found in the elemental reconstructions of the embryo at 24 hpf.[10] In contrast to the notochord, the myotome appears to be Fe-rich and a distinct accumulation of Zn is found at the tip of the tail. Both features are in agreement with the previously reported elemental distributions of the 24 hpf embryo at the onset of the pharyngula period.[10]

Conclusions

Zebrafish embryogenesis is characterized by a succession of complex morphological changes that are accompanied by a dynamic reorganization of the trace metal distribution. With the goal of mapping out the 3-dimensional organization of Zn, Fe, and Cu at key stages of embryonic development, the current data set complements our previously reported tomographic elemental analysis at 24 hpf,[10] and offers first insights into the distribution of Zn and Fe at the onset of the hatching period at 48 hpf. Notably, the volumetric data set revealed increased concentrations of Zn throughout yolk and the tip of the tail, thus mirroring the distribution at 24 hpf. In addition, both developmental stages showed increased levels of Fe throughout the brain and along the posterior body. In contrast to the preceding pharyngula period, regions of the brain as well as the liver and heart are now well delineated.

Future work is required to gauge the effect of chemical fixation and low-temperature embedding on altering the trace metal content in zebrafish. The low Fe levels in the yolk certainly raise the question to what extent the employed embedding protocol might alter the trace metal contents, especially with regard to extracellular fluids. While cryo-fixation and data acquisition at liquid nitrogen temperature would be the method of choice to preserve the native trace metal composition, this approach poses significant technical difficulties when employed for this size of specimen. Furthermore, tomographic mapping of the Cu distribution remains challenging due to the low signal-to-noise ratio achieved for this element. In most organisms, the total Cu content is at least one order of magnitude lower compared to Fe and Zn, thus posing higher demands on the instrument sensitivity. Although the Fresnel zone plate optics of the current instrument is capable of focusing the beam to a submicron-sized spot, there is currently no benefit for such high spatial resolution with specimens as large as a zebrafish embryo due to prohibitively long data acquisition times.

In summary, X-ray fluorescence microtomography is well suited to visualize trace metal distributions in embedded specimens of the size of a zebrafish embryo. By further expanding 3D elemental imaging studies to other key stages of embryonic development, we anticipate to unravel the complex dynamics of trace metal redistribution in the course of organ development during the first 3 days of embryogenesis in a comprehensive fashion.

Acknowledgements

Financial support by the National Science Foundation (CHE-1306943) is gratefully acknowledged. Use of the Advanced Photon Source was supported by the U.S. Department of Energy, Office of Science, Office of Basic Energy Sciences, under Contract No. DE-AC02-06CH11357.

Notes and references

1 M. Huesca, L. S. Lock, A. A. Khine, S. Viau, R. Peralta, I. H. Cukier, H. N. Jin, R. A. Al-Qawasmeh, Y. Lee, J. Wright and A. P. Young, *Mol. Cancer Ther.*, 2009, **8**, 2586; J. K. Chesters and L. Petrie, *J. Nutr. Biochem.*, 1999, **10**, 279; J. K. Chesters, L. Petrie and K. E. Lipson, *J. Cell. Physiol.*, 1993, **155**, 445; L. Sun, Y. Chai, R. Hannigan, V. K. Bhogaraju and K. Machaca, *J. Cell. Physiol.*, 2007, **213**, 98; M. L. Bernhardt, A. M. Kim, T. V. O'Halloran and T. K. Woodruff, *Biol. Reprod.*, 2011, **84**, 526; B. Y. Kong, F. E. Duncan, E. L. Que, A. M. Kim, T. V. O'Halloran and T. K. Woodruff, *Mol. Hum. Reprod.*, 2014, **20**, 1077; E. L. Que, R. Bleher, F. E. Duncan, B. Y. Kong, S. C. Gleber, S. Vogt, S. Chen, S. A. Garwin, A. R. Bayer, V. P. Dravid, T. K. Woodruff and T. V. O'Halloran, *Nat. Chem.*, 2015, **7**, 130.

2 G. Terrin, R. Berni Canani, M. Di Chiara, A. Pietravalle, V. Aleandri, F. Conte and M. De Curtis, *Nutrients*, 2015, **7**, 10427; M. S. Azman, W. S. W. Saudi, M. Ilhami, M. S. A. Mutalib and M. T. Rahman, *Nutr. Neurosci.*, 2009, **12**, 9.

3 L. Gambling, C. Kennedy and H. J. McArdle, *Semin. Cell Dev. Biol.*, 2011, **22**, 637; C. L. Keen, J. Y. Uriu-Hare, S. N. Hawk, M. A. Jankowski, G. P. Daston, C. L. Kwik-Uribe and R. B. Rucker, *Am. J. Clin. Nutr.*, 1998, **67**, 1003S; J. Y. Uriu-Adams, R. E. Scherr, L. Lanoue and C. L. Keen, *Biofactors*, 2010, **36**, 136.

4 S. Ma, S.-G. Lee, E. B. Kim, T. J. Park, A. Seluanov, V. Gorbunova, R. Buffenstein, J. Seravalli and V. N. Gladyshev, *Cell Rep.*, 2015, **13**, 1319.

5 R. L. Miyares, V. B. de Rezende and S. A. Farber, *Dis. Mod. Mech.*, 2014, **7**, 915.

6 M. Westerfield, *The zebrafish book. A guide for the laboratory use of zebrafish (Danio rerio)*, University of Oregon Press, Eugene, 2000.

7 C. B. Kimmel, W. W. Ballard, S. R. Kimmel, B. Ullmann and T. F. Schilling, *Dev. Dyn.*, 1995, **203**, 253.

8 M. J. Pushie, I. J. Pickering, M. Korbas, M. J. Hackett and G. N. George, *Chem Rev*, 2014, **114**, 8499; C. J. Fahrni, *Curr. Opin.*

Chem. Biol., 2007, **11**, 121; R. McRae, P. Bagchi, S. Sumalekshmy and C. J. Fahrni, *Chem. Rev.*, 2009, **109**, 4780; D. J. Hare, E. J. New, M. D. de Jonge and G. McColl, *Chem. Soc. Rev.*, 2015, **44**, 5941.

9 M. D. de Jonge, C. Holzner, S. B. Baines, B. S. Twining, K. Ignatyev, J. Diaz, D. L. Howard, D. Legnini, A. Miceli, I. McNulty, C. J. Jacobsen and S. Vogt, *Proc. Natl. Acad. Sci. USA*, 2010, **107**, 15676; M. D. de Jonge and S. Vogt, *Curr. Opin. Struct. Biol.*, 2010, **20**, 606; E. Lombi, M. D. de Jonge, E. Donner, P. M. Kopittke, D. L. Howard, R. Kirkham, C. G. Ryan and D. Paterson, *Plos One*, 2011, **6**; G. McColl, S. A. James, S. Mayo, D. L. Howard, C. G. Ryan, R. Kirkham, G. F. Moorhead, D. Paterson, M. D. de Jonge and A. I. Bush, *PLoS One*, 2012, **7**, e32685.

10 D. Bourassa, S.-C. Gleber, S. Vogt, H. Yi, F. Will, H. Richter, C. H. Shin and C. J. Fahrni, *Metallomics*, 2014, **6**, 1648.

11 R. Bryson-Richardson, S. Berger and P. Currie, *Atlas of Zebrafish Development*, Elsevier Science, 2011.

12 N. Hu, D. Sedmera, H. J. Yost and E. B. Clark, *Anatom. Rec.*, 2000, **260**, 148.

13 R. Dahm, H. B. Schonthaler, A. S. Soehn, J. Van Marle and G. Vrensen, *Exp. Eye Res.*, 2007, **85**, 74.

14 B. L. Armbruster, E. Carlemalm, R. Chiovetti, R. M. Garavito, J. A. Hobot, E. Kellenberger and W. Villiger, *J. Microsc.*, 1982, **126**, 77; E. Carlemalm, R. M. Garavito and W. Villiger, *J. Microsc.*, 1982, **126**, 123.

15 S. Vogt, *J. Phys. IV*, 2003, **104**, 635.

16 MATLAB, Mathworks, Natick, MA, 2012.

17 U. Ayachit, *The ParaView Guide: A Parallel Visualization Application*, 2015, ISBN 978-1930934306.

18 W. S. Rasband, ImageJ, National Institutes of Health, Bethesda, Maryland, USA, http://imagej.nih.gov/ij/, 1997-2016.

19 L. Perrin, A. Carmona, S. Roudeau and R. Ortega, *J. Anal. At. Spectrom.*, 2015, **30**, 2525.

20 S. J. Nixon, R. I. Webb, M. Floetenmeyer, N. Schieber, H. P. Lo and R. G. Parton, *Traffic*, 2009, **10**, 131.

21 S. Matsuyama, M. Shimura, M. Fujii, K. Maeshima, H. Yumoto, H. Mimura, Y. Sano, M. Yabashi, Y. Nishino and K. Tamasaku, *X-ray Spectrom.*, 2010, **39**, 260; S. A. James, D. E. Myers, M. D. de Jonge, S. Vogt, C. G. Ryan, B. A. Sexton, P. Hoobin, D. Paterson, D. L. Howard, S. C. Mayo, M. Altissimo, G. F. Moorhead and S. W. Wilkins, *Anal. Bioanal. Chem.*, 2011.

22 R. Reichelt, E. Carlemalm, W. Villiger and A. Engel, *Ultramicroscopy*, 1985, **16**, 69.

23 E. Ho, S. Dukovcic, B. Hobson, C. P. Wong, G. Miller, K. Hardin, M. G. Traber and R. L. Tanguay, *Comp. Biochem. Physiol. C*, 2012, **155**, 26.

24 B. M. Weinstein, A. F. Schier, S. Abdelilah, J. Malicki, L. Solnica-Krezel, D. L. Stemple, D. Y. Stainier, F. Zwartkruis, W. Driever and M. C. Fishman, *Development*, 1996, **123**, 303; K. Kulkeaw and D. Sugiyama, *Stem Cell Res. Ther.*, 2012, **3**, 1.

25 A. Donovan, A. Brownlie, Y. Zhou, J. Shepard, S. J. Pratt, J. Moynihan, B. H. Paw, A. Drejer, B. Barut, A. Zapata, T. C. Law, C. Brugnara, P. D. Kingsley, J. Palis, M. D. Fleming, N. C. Andrews and L. I. Zon, *Nature*, 2000, **403**, 776; S. P. Mudumana, H. Y. Wan, M. Singh, V. Korzh and Z. Y. Gong, *Dev. Dyn.*, 2004, **230**, 165.

26 S. Ben-Horin, A. Shinfeld, E. Kachel, A. Chetrit and A. Livneh, *Am. J. Med.*, 2005, **118**, 636.

27 H. A. Field, E. A. Ober, T. Roeser and D. Y. R. Stainier, *Dev. Biol.*, 2003, **253**, 279.

28 P. M. Harrison and P. Arosio, *Biochim. Biophys. Acta*, 1996, **1275**, 161.

29 P. Arosio, F. Carmona, R. Gozzelino, F. Maccarinelli and M. Poli, *Biochem J*, 2015, **472**, 1.

30 K. A. Soules and B. A. Link, *BMC Dev. Biol.*, 2005, **5**.

31 W. Y. Chen, J. A. C. John, C. H. Lin, H. F. Lin, S. C. Wu, C. H. Lin and C. Y. Chang, *Aquat. Toxicol.*, 2004, **69**, 215.

32 M. Ugarte, N. N. Osborne, L. A. Brown and P. N. Bishop, *Surv. Opth.*, 2013, **58**, 585; H. Ripps and R. L. Chappell, *Mol. Vision*, 2014, **20**, 1067.

33 T. Akagi, M. Kaneda, K. Ishii and T. Hashikawa, *J. Histochem. Cytochem.*, 2001, **49**, 87; I. Lengyel, J. M. Flinn, T. Peto, D. H. Linkous, K. Cano, A. C. Bird, A. Lanzirotti, C. J. Frederickson and F. J. G. M. van Kuijk, *Exp. Eye Res.*, 2007, **84**, 772.

34 X. Wang, Z.-Y. Wang, H.-L. Gao, G. Danscher and L. Huang, *Brain Res. Bull.*, 2006, **71**, 91.

35 S. Redenti and R. L. Chappell, *Vision Res.*, 2004, **44**, 3317.

36 S. J. Yin, C. F. Chou, C. L. Lai, S. L. Lee and C. L. Han, *Chem. Biol. Inter.*, 2003, **143**, 219; A. M. Huber and S. N. Gershoff, *J. Nutr.*, 1975, **105**, 1486.

37 S. Redenti and R. L. Chappell, *Vision Res.*, 2005, **45**, 3520.

38 M. Ugarte, G. W. Grime, G. Lord, K. Geraki, J. F. Collingwood, M. E. Finnegan, H. Farnfield, M. Merchant, M. J. Bailey, N. I. Ward, P. J. Foster, P. N. Bishop and N. N. Osborne, *Metallomics*, 2012, **4**, 1245.

39 G. Moiseyev, Y. Takahashi, Y. Chen, S. Gentleman, T. M. Redmond, R. K. Crouch and J. X. Ma, *J. Biol. Chem.*, 2006, **281**, 2835.

40 M. T. Rajan, K. S. J. Rao, B. M. Mamatha, R. V. Rao, P. Shanmugavelu, R. B. Menon and M. V. Pavithran, *J. Neurol. Sci.*, 1997, **146**, 153; H. Duflou, W. Maenhaut and J. Dereuck, *Neurochem. Res.*, 1989, **14**, 1099.

41 B. F. G. Popescu, C. A. Robinson, A. Rajput, A. H. Rajput, S. L. Harder and H. Nichol, *Cerebellum*, 2009, **8**, 74.

42 J. Beard, *J. Nutr.*, 2003, **133**, 1468S; B. K. Y. Bitanihirwe and M. G. Cunningham, *Synapse*, 2009, **63**, 1029.

43 J. L. Beard, J. R. Connor and B. C. Jones, *Nutr. Rev.*, 1993, **51**, 157.

44 J. R. Connor, S. L. Menzies, S. M. Stmartin and E. J. Mufson, *J. Neurosci. Res.*, 1990, **27**, 595.

45 E. M. Taylor and E. H. Morgan, *Dev. Brain. Res.*, 1990, **55**, 35.

46 M. M. Braga, D. B. Rosemberg, D. L. de Oliveira, C. M. Loss, S. D. Córdova, E. P. Rico, E. S. Silva, R. D. Dias, D. O. Souza and M. E. Calcagnotto, *Zebrafish*, 2013, **10**, 376.

47 D. L. Stemple, *Development*, 2005, **132**, 2503; J. P. Kanki and R. K. Ho, *Development*, 1997, **124**, 881.

A detailed knowledge of the spatial organization of trace metals in cells and tissues is of critical importance for understanding their role during early embryonic development where morphological changes occur with rapid succession. Such a three-dimensional atlas also offers a valuable framework for the correlation with other experimental data such as the spatio-temporal dynamics of gene expression during development. Taking advantage of microXRF tomography, the present study offers new insights into the trace metal distribution during the hatching period, a key stage in zebrafish embryogenesis where the heart, liver, and distinct features of the lens and retina are taking shape.